catalysts

MDPI

Article

# Effect of Dopant Loading on the Structural and Catalytic Properties of Mn-Doped $SrTiO_3$ Catalysts for Catalytic Soot Combustion

**Santiago Iván Suárez-Vázquez [1,*], Arquímedes Cruz-López [1], Carlos Eduardo Molina-Guerrero [1], Astrid Iriana Sánchez-Vázquez [2] and Carlos Macías-Sotelo [1]**

[1] Universidad Autónoma de Nuevo León, Facultad de Ingeniería Civil, Av. Universidad S/N, Cd. Universitaria, San Nicolás de los Garza 66455, Nuevo León, Mexico; cruz_lopeza@yahoo.com.mx (A.C.-L.); molinaguerreroce@gmail.com (C.E.M.-G.); macvel112@hotmail.com (C.M.-S.)

[2] Universidad Autónoma de Nuevo León, Facultad de Ciencias Químicas, Av. Universidad S/N, Cd. Universitaria, San Nicolás de los Garza 66455, Nuevo León, Mexico; asirisan@yahoo.com.mx

* Correspondence: ssuarezvazquez@gmail.com or santiago.suarezvz@uanl.edu.mx

Received: 20 December 2017; Accepted: 5 February 2018; Published: 9 February 2018

**Abstract:** Soot particles have been associated with respiratory diseases and cancer. To decrease these emissions, perovskite-mixed oxides have been proposed due to their thermal stability and redox surface properties. In this work, $SrTiO_3$ doped with different amounts of Mn were synthesized by the hydrothermal method and tested for soot combustion. Results show that at low Mn content, structural distortion, and higher $O_{ads}/O_{lat}$ ratio were observed which was attributed to the high content of $Mn^{3+}$ in Ti sites. On the other hand, increasing the Mn content led to surface segregation of manganese oxide. All synthesized catalysts showed mesopores in the range of 32–47 nm. In the catalytic combustion of soot, the samples synthesized in this work lowered the combustion temperature by more than 100 °C compared with the uncatalyzed reaction. The sample doped with 1 wt % of Mn showed the best catalytic activity. The activation energy of these samples was also calculated, and the order of decreasing activation energy is as follows: uncatalyzed > Mn0 > Mn8 > Mn4 > Mn1. The best catalytic activity for Mn1 was attributed to its physicochemical properties and the mobility of the oxygen from the bulk to the surface at temperatures higher than 500 °C.

**Keywords:** activation energy; hydrothermal synthesis; catalytic combustion; soot; perovskite

## 1. Introduction

Recently, demand for diesel engines has been increasing. Unfortunately, the use of these engines is associated with large amounts of atmospheric emissions. Efforts to reduce of $NO_x$ and particulate matter in these emissions have been attracting more and more attention in the scientific community. In particular, fine soot particles have been associated with respiratory diseases and premature death by cancer [1]. In addition, the US-EPA has shown that soot particles are correlated with lung cancer in humans [2]. For this reason, governments around the world have been working to curb these emissions [3]. Diesel particulate filters with oxidation catalysis is, so far, the most promising technique to solve this problem. It is well known the combustion temperature of soot is approximately 700 °C, which is much higher than the typical temperature in the diesel exhaust. Noble metal catalysts such as Pt and Pd have acceptable reported efficiencies [4–6]; however, their high cost and deactivation due to coke formation compels us to seek alternatives.

A new alternative is the use of transition metal oxides with perovskite structure which have been used as catalysts for soot and volatile organic compounds [7–16] or photocatalysts mainly related with

the remotion of organic compounds [17,18]. Most perovskites, in particular $SrTiO_3$, are characterized by high thermal stability, oxidative properties, and low cost, which make them good candidates for catalysts [7]. Recently, perovskites with the general structure $ABO_3$, with different values of A or B, have been used as catalysts in soot oxidation reactions. Lopez-Suarez et al. reported that $SrTiO_3$ impregnated with Cu and synthesized by the sol-gel method showed the highest catalytic activity over $Cu/MgTiO_3$ and other supports, decreasing the combustion temperature by approximately 10%. They attributed this behavior to weakly bound oxygen, which was promoted by the Cu-$SrTiO_3$ interactions [8]. Later, the same group reported that lattice copper in $SrTiCuO_3$ promotes the $NO_x$ chemisorption and oxidation capacity which is associated with the best catalytic activity during soot oxidation decreasing the combustion temperature by approximately 30% comparing the uncatalyzed reaction [9]. Feng et al. reported the doping by Ce and Co in $LaFeO_3$. They observed an increase in the redox property by adding 6 at % of Ce in A site and 12 at % Co in B site. However, excessive levels of these metals inhibited the improvement in the catalytic activity due to the formation of $CeO_2$ and $Co_3O_4$ [10]. Later, the same group prepared $La_{0.8}Ce_{0.2}Mn_{1-x}Fe_xO_3$ impregnated with K. They observed that partial modification of B site by adding Fe promotes the redox properties of the catalyst while K on the surface enhances the formation of oxygen active species both increasing the catalytic activity [11]. Pecchi et al. studied the same perovskite mentioned above ($LaMnO_3$), however they partially substituted the A and B sites to prepare $La_{1-x}Ag_xMn_{0.9}Co_{0.1}O_3$. They reported that the presence of Ag in the A site promotes the formation of oxygen vacancies that are associated with higher oxygen adsorption, enhancing the catalytic activity [12]. Hernandez et al. worked with $La_{0.6}Sr_{0.4}BO_3$ where B = Fe, Mn, and Ti prepared by thermal decomposition route. The sample with Mn showed the best catalytic activity during the soot oxidation reaction. They attributed this behavior to the $Mn^{4+}$ species, which can be locally reduced by transporting oxygen to the catalyst–soot interface [13].

As described above, changing A or B sites in perovskites modifies its redox properties, which can improve catalytic activity. In addition, it is well known that Ti or B site in perovskite structure can be as $Ti^{4+}$ or $Ti^{3+}$ or its redox pair depending the metal in the A site or the existence of defects in the perovskite [19–22]. Additionally, for $SrTiO_3$, different metal can be incorporated as a metal dopant in the B site, making it a good candidate for soot oxidation [8,9]. On the other hand, $LaMnO_3$ has a similar structure and can also work as a catalyst in this reaction due the different Mn species in the B site [13]. For these reasons, and considering the different species of Mn, $SrTiO_3$ doped by Mn in Ti sites was tested as catalysts in soot combustion. Mn was used as a dopant to promote the formation of structural defects in the perovskite catalyst. Samples obtained in this work have a peculiar dendritic morphology with high surface area to improve the catalyst–soot contact and enhance its catalytic activity.

## 2. Results and Discussion

Figure 1 shows X-ray diffractograms for catalysts prepared in this study. All samples show the formation of $SrTiO_3$ with a cubic structure and a theoretical lattice parameter of 3.8980 Å, according to PDF-01-084-0443 (Figure 1a). In addition, some impurities of $SrCO_3$ are observed in all samples. It is well known that the carbonate species can be formed if the hydroxides or SrO are in contact with atmospheric $CO_2$ during the hydrothermal reaction [7,23]. No evidence of $MnO_x$ is detected, indicating the possible incorporation of Mn into the $SrTiO_3$ lattice. Figure 1b shows an enlargement of the peak located at 32.45° in $2\theta$. A slight shift to higher angles is observed in samples doped by 1 wt % Mn. However, at higher Mn content, the position of the peak returns to low angles. This behavior could indicate high structural distortion produced by different ionic radius to the metal dopant as was previously reported for these samples [17,18]. In addition, Table 1 shows crystallite size calculated using the peak shown in Figure 1b. A slight decrease is observed by adding 1 wt % of Mn, followed by an increase as the Mn content increases. This table also shows the lattice parameters calculated for all catalysts synthesized in this work. A slight decrease in the lattice parameter is observed for the Mn1 sample confirming the structural distortion in this sample. When the content of Mn is increased (Mn8 sample), the lattice parameter returns to its original value (undoped sample Mn0). It is worth

mentioning that Mn0 sample has similar lattice parameters to the theoretical parameters reported in the XRD card mentioned above. The ICP results shown in Table 1 confirm the total content of Mn in each sample, which were very close to the theoretical values. From these results, it is feasible to deduce that structural distortion is mainly produced at lower amounts of Mn dopant [17].

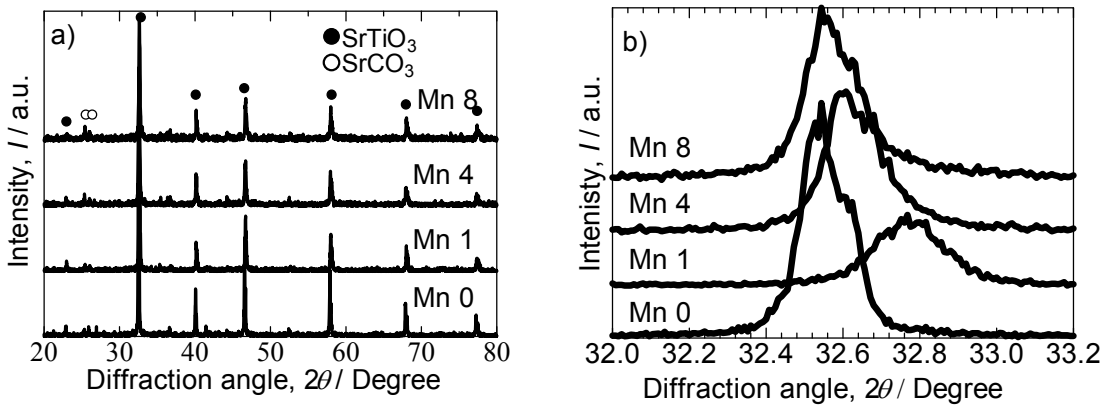


**Figure 1.** (**a**) X-ray diffractograms and (**b**) zoom-in of the peak located at 32.45° of catalysts with different contents of Mn synthesized in this work by hydrothermal method and calcined at 600 °C for 5 h.

**Table 1.** Crystallite size calculated by XRD and content of Mn obtained by ICP analysis of catalysts synthesized in this work.

| Sample | Crystallite Size (nm) | Mn (wt %) | Lattice Parameter (Å) |
|---|---|---|---|
| Mn0 | 63.7 | 0.09 ± 0.07 | 3.886 |
| Mn1 | 39.5 | 1.97 ± 0.05 | 3.862 |
| Mn4 | 54.1 | 4.26 ± 0.02 | 3.881 |
| Mn8 | 53.8 | 8.98 ± 0.05 | 3.887 |

The morphology of catalysts is observed in Figure 2, which is a representative image of all samples synthesized in this work. No difference was observed among samples despite the different amounts of Mn. Dendritic morphology is clearly detected for all samples; dendrites are composed by a main long branch approximately 0.5 μm in length. The formation of dendrites is associated with the diffusion process during the hydrothermal reaction [24,25]. Figure 2c,d show the elemental surface concentration of samples shown in Figure 2a,b. It is clearly observed that the surface for sample Mn0 is absent any Mn (Figure 2d), but in sample Mn4, some content of Mn below the 4 wt % is detected. The remaining Mn content should be incorporated into the structure in the A or B sites of $ABO_3$. The experimental ratio Sr/Ti is 2.03 and 1.56 for Mn4 and Mn0, respectively, which are very close to the theoretical values of 2.13 and 1.81 assuming that Mn occupies Ti sites in the Mn4 sample.

Surface characterization was carried out by XPS. Figure 3a shows Mn $2p^{3/2}$ spectra in the range 626–648 eV, and the deconvolution analysis of the samples synthesized in this work. It is clearly observed that higher intensity peaks indicate higher amounts of Mn as expected. From the deconvolution analysis, two well-defined peaks are clearly observed at 641.5 and 642.9 eV. However, the sample doped by 8 wt % Mn showed a displacement to lower binding energies, with peaks at 640.9 and 641.8 eV. The earlier peaks are related to the existence of $Mn^{3+}$ and $Mn^{4+}$ on the surface of the catalyst while the latter could be associated with the formation of $Mn^{2+}$ and $Mn^{3+}$ on the surface of the Mn8 sample [13,26]. This behavior agrees well with the slight displacement to higher angles observed in Figure 1b for Mn1 sample, which can be associated with the differences in ionic radii among species. It is well known that $Mn^{3+}$ has an ionic radius of 72 Å, which is very similar to that reported for $Ti^{4+}$ (74 Å). However, $Mn^{4+}$ has a lower ionic radius (67 Å) than $Ti^{4+}$ and $Mn^{3+}$; this different size can

explain the distortion observed in Figure 1b. On the other hand, the higher $Mn^{3+}/Mn^{4+}$ ratio in the Mn1 sample obtained by XPS (Table 2) can promote the formation of structural defects, such as oxygen vacancies in the perovskite catalyst, due to the loss of charge neutrality after the substitution of $Mn^{3+}$ in $Ti^{4+}$ sites. These defects can also be related to the distortion observed in Figure 1b by XRD. The smaller crystallite size and the lattice parameter shown in Table 1 for this sample (Mn1) confirm this discussion. In contrast, the high content of Mn in sample Mn8 resulted in the formation of $Mn^{3+}$ with small percentage of $Mn^{2+}$ (0.81 Å) located on the surface of the catalyst, likely as $Mn_3O_4$ or MnO, but not into the structure as Mn1. For this reason, the distortion in Figure 1b decreases for Mn8 having the same 2θ value than Mn0 with similar lattice parameter (Table 1). Figure 3b also confirms the discussion mentioned above. Figure 3b shows the O *1s* spectra obtained by XPS. The deconvolution analysis shows two well defined peaks in all samples located at 528.8 and 530.6 eV, which are respectively attributed to lattice oxygen ($O_{lat}$) from the perovskite structure or surface segregated oxides and surface adsorbed oxygen ($O_{ads}$), associated with defect oxides [27], carbonates or hydroxyl species, as well as weakly bonded oxygen adsorbed on the surface [13,26]. The $O_{ads}/O_{lat}$ ratio shown in Table 2 demonstrates high $O_{ads}$ in the Mn1 sample, which can be attributed to the structural defects produced by the $Mn^{3+}/Mn^{4+}$ ratio shown in Table 2 [1]. On the other hand, the Mn8 sample shows higher $O_{lat}$, attributable to manganese oxides segregated on the surface of the catalyst, confirming a lower degree of distortion (Figure 1b) and the formation of $Mn^{2+}$ (Figure 3a).

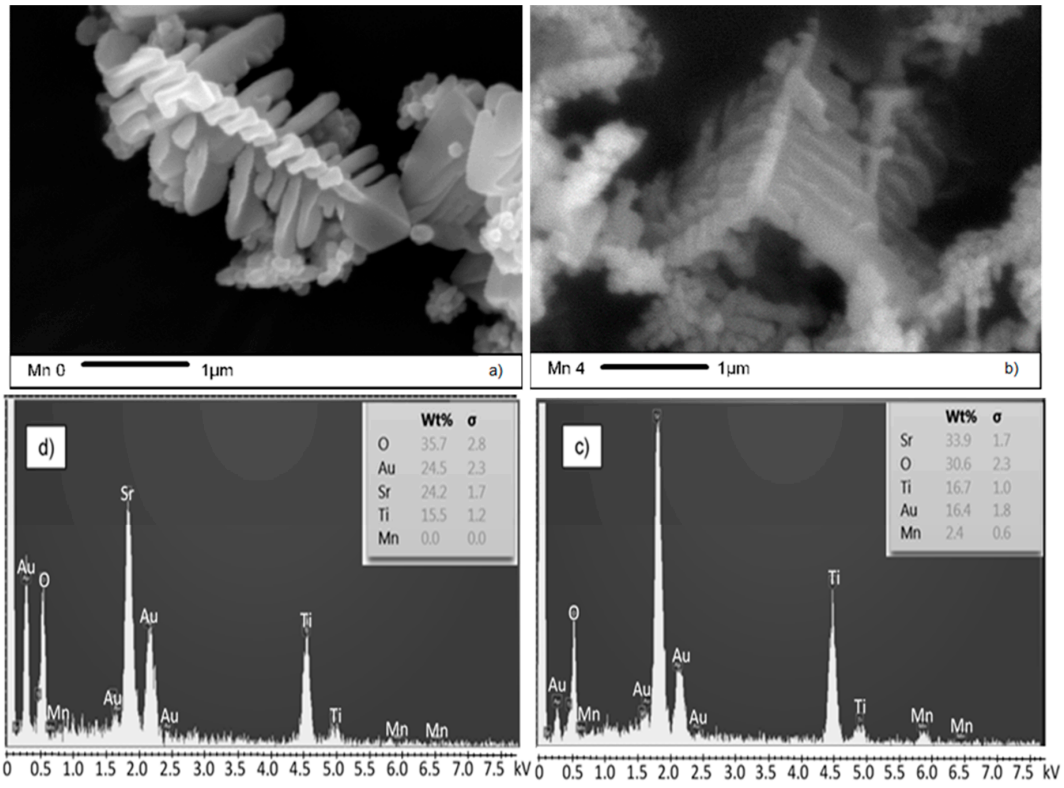


**Figure 2.** (**a**) Mn0 and (**b**) Mn4 SEM images of catalysts with dendritic morphology; (**c**) Mn4 and (**d**) Mn0 EDS spectra of samples synthesized in this work by hydrothermal method and calcined at 600 °C for 5 h.

Figure 4 shows the $N_2$ adsorption–desorption isotherms. All samples have typical type IV isotherm showing a hysteresis loop at high relative pressures, which is associated with capillary condensation representative of mesoporous materials [24–28]. This is confirmed by the mean pore size shown in Table 2, where all samples have a pore size in the range of mesopores (2–50 nm). Table 2 also shows the pore volume of approximately 0.12–0.16 $cm^3 \cdot g^{-1}$ and surface areas of above 11 $m^2 \cdot g^{-1}$.

These results are slightly higher than values previously reported for perovskite type catalysts for soot oxidation reactions [8,16,22], which is attributed to the dendritic morphology observed in Figure 2. Based on these results, it is expected that perovskites synthesized in this work can be used as catalysts in the soot combustion reaction.

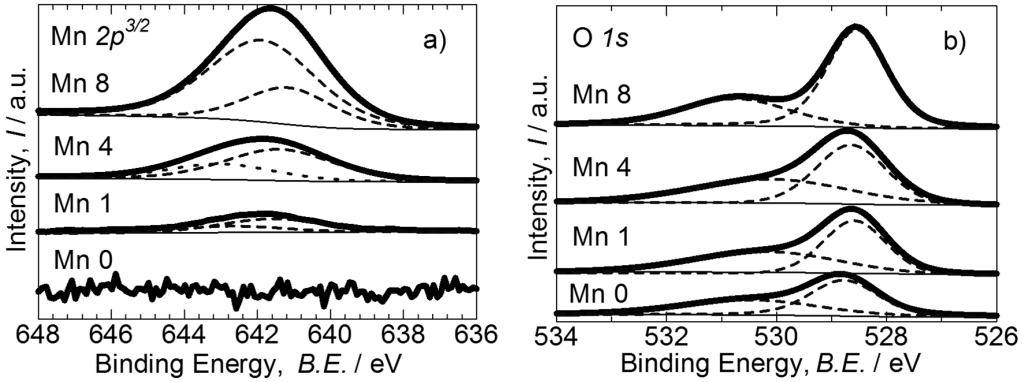


**Figure 3.** XPS spectra of catalysts with different contents of Mn synthesized in this work by hydrothermal method and calcined at 600 °C for 5 h (**a**) Mn $2p^{3/2}$ (**b**) O *1s*.

**Table 2.** Textural and superficial properties of catalysts synthesized in this work.

| Sample | Mean Pore Size (nm) | Pore Volume ($cm^3 \cdot g^{-1}$) | Surface Area ($m^2 \cdot g^{-1}$) | $O_{ads}/O_{lat}$ | $Mn^{3+}/Mn^{4+}$ |
|---|---|---|---|---|---|
| Mn0 | 41.9 | 0.123 | 11.7 | 0.84 | - |
| Mn1 | 32.3 | 0.140 | 17.4 | 0.94 | 2.30 |
| Mn4 | 42.5 | 0.156 | 14.6 | 0.89 | 2.15 |
| Mn8 | 46.8 | 0.123 | 10.9 | 0.48 | 3.09 * |

* This value corresponds to the $Mn^{3+}/Mn^{2+}$ ratio according to results shown in Figure 3a.

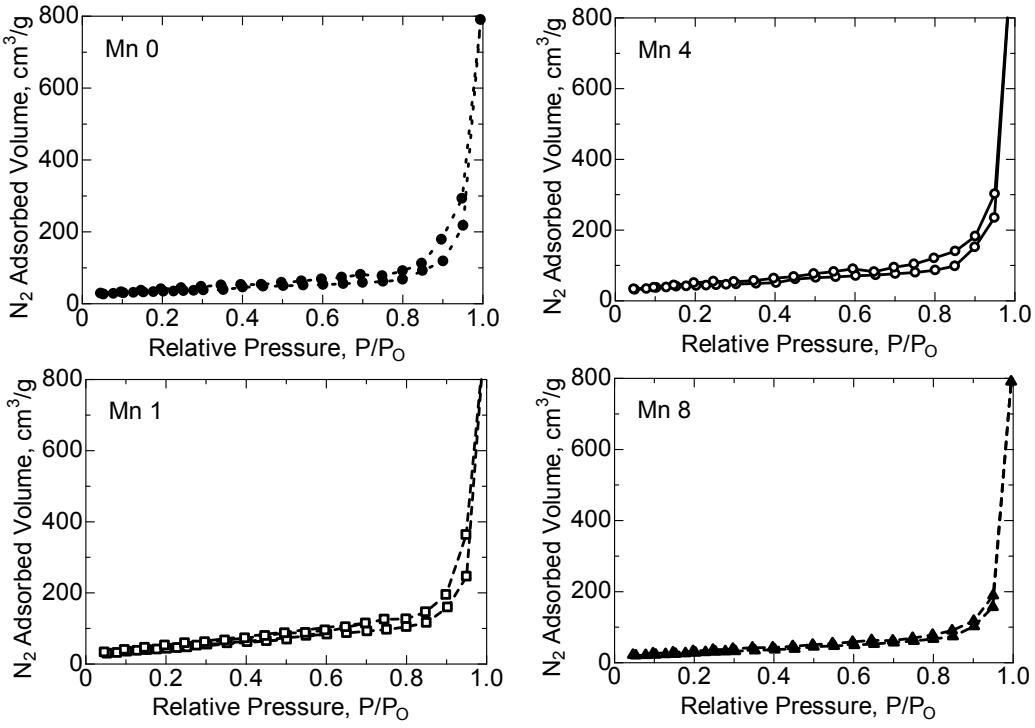


**Figure 4.** $N_2$ adsorption–desorption isotherms of samples with different contents of Mn synthesized in this work by hydrothermal method and calcined at 600 °C for 5 h.

Figure 5a shows the DTG profiles obtained during the catalytic decomposition of soot using the catalysts synthesized in this study. This figure shows a clear decrease in the temperature of the maximum peak ($T_m$) for catalyzed reactions compared with the control, un-catalyzed reaction. The $T_m$ of the soot combustion reactions in decreasing order are as follows: uncatalyzed > Mn0 > Mn8 > Mn4 > Mn1. The catalyst Mn1 had the lowest $T_m$ at 591 °C, decreasing the temperature more than 100 °C compared with the un-catalyzed sample (700 °C). Notably, the soot model used in this study, carbon Vulcan, has a higher combustion temperature than Printex U. All $T_m$ data are shown in Table 3. The highest difference in $T_m$, at approximately 26 °C, occurred between the Mn1 and Mn0 catalysts, and is similar to previous reports, where different doped perovskites were used [16,29,30]. In addition, the most effective catalyst tested in this study is that one doped with 1 wt % of Mn (Mn1), which lowered the catalytic combustion of soot to 591 °C. This result is comparable with different perovskites where the $T_m$ of soot combustion reached temperatures above 500 °C [9,22,31,32]. Table 4 shows a comparison of $T_m$'s for some perovskites, including $SrTiO_3$ and Cu doped $SrTiO_3$ prepared by different routes [22]. As shown in Table 4, the perovskites synthesized in this work have comparable $T_m$ values with previous reports, which is attributed to higher surface area and the dendritic morphology of these catalysts. These characteristics promote increased contact between catalyst and soot particles. These phenomena were previously observed by Lee C. et al. [32] who reported that a perovskite with a three-dimensional fiber network structure can improve the contact among reactants, therefore decreasing the combustion temperature. It is worth mentioning that increasing the amount of Mn leads to an increase in the $T_m$. This is likely due to fewer structural defects in the catalysts as indicated by the $O_{ads}/O_{lat}$ ratio as well as the existence of a reduced species of Mn, such as $Mn^{2+}$ in the Mn8 sample. The quantification of the catalytic effect of samples in soot combustion was calculated by the $E_a$ using Equation (2) and is shown in Figure 5b. A larger slope is observed for Mn0 and un-catalyzed samples indicating their low catalytic activity. As shown in Table 4, the lowest $E_a$ is calculated for Mn1, which is associated with the higher $O_{ads}/O_{lat}$ and $Mn^{3+}/Mn^{4+}$ ratios shown in Table 2 [3]. Finally, Figure 5c shows the TGA results of all catalysts synthesized in this work. A loss in mass is clearly observed at low temperatures (<500 °C) for samples Mn0 and Mn8 but not for Mn1, indicating that Mn0 and Mn8 are active at lower temperatures. This behavior can be explained as statement in the literature [13]. In the case of Mn8, segregated $Mn_3O_4$ promotes the adsorption of oxygen (Figure 3). The adsorbed oxygen starts to reacts with soot at temperatures below 500 °C, and an increment in the mass loss, attributed to the soot combustion, is clearly detected. In contrast, the preservation of the perovskite structure with high $Mn^{3+}$ content in Mn1 and Mn4, which correlates with the formation of surface oxygen vacancies, can produce a competing oxidation reaction between soot combustion and the oxidation of $Mn^{3+}$ to $Mn^{4+}$, resulting in rapidly filled surface oxygen vacancies and low mass loss (see Figure 5c), as described by Xueting et al. [27]. However, at temperatures higher than 500 °C, oxygen migrates from the bulk to the catalyst surface. The Mn1 sample, rich in structural defects (as shown in Figure 3b), is the best catalyst for oxygen transportation via the ion-mobility mechanism [13,27], which promotes the combustion of soot. Mass loss increases dramatically as a consequence. The driving force can be the oxygen gradient produced in the interface between soot-catalyst and the bulk.

**Table 3.** $T_m$ and activation energy for the catalysts synthesized in this work during the soot catalytic reaction.

| Sample | $T_m$ (°C) | $E_a$ (kJ·K$^{-1}$·mol$^{-1}$) |
|---|---|---|
| Uncatalyzed | 700 | 133.45 |
| Mn0 | 617 | 109.01 |
| Mn1 | 591 | 87.28 |
| Mn4 | 605 | 102.97 |
| Mn8 | 614 | - |

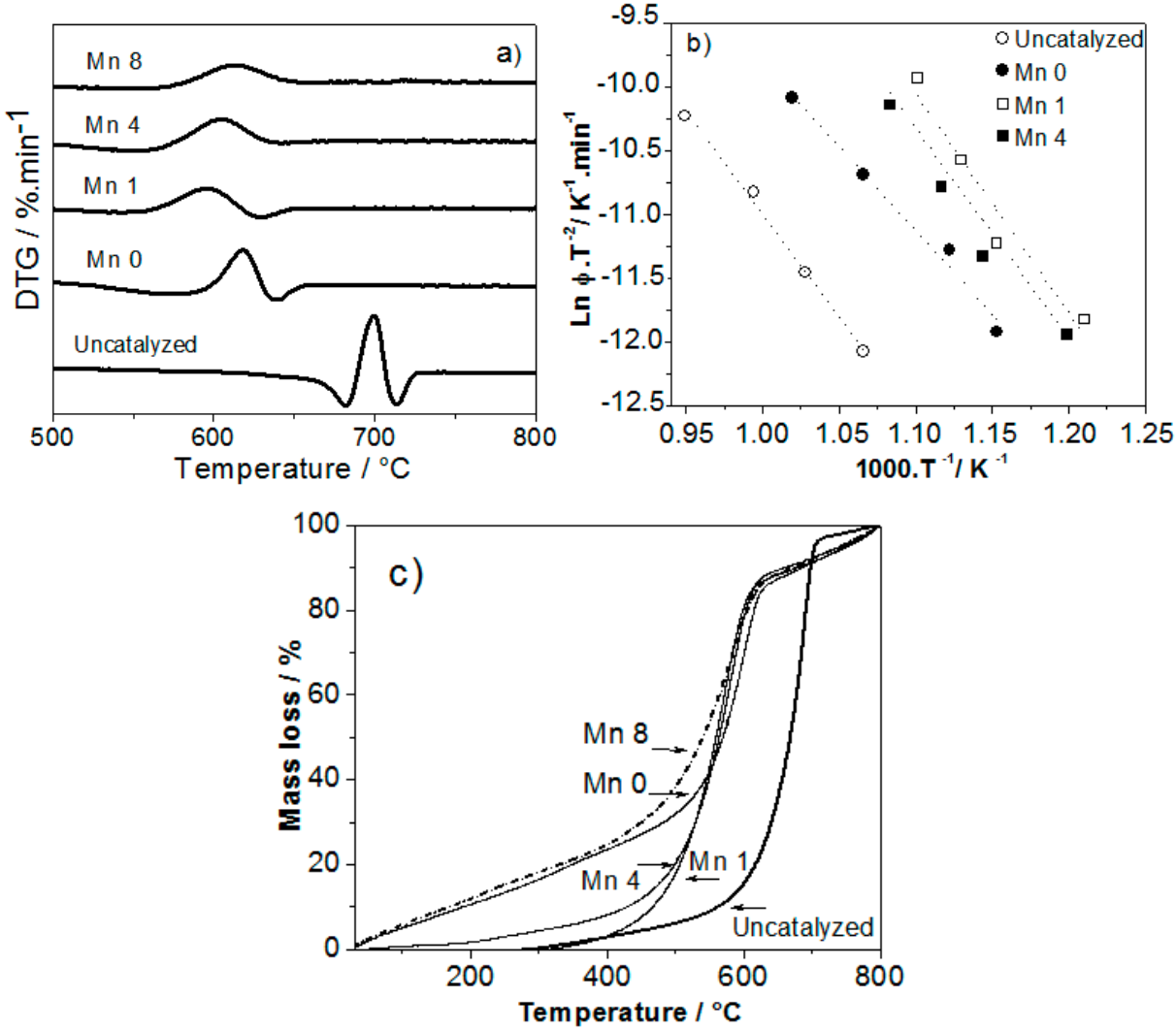


**Figure 5.** Soot catalytic reaction using catalysts synthesized in this work with different contents of Mn. (**a**) DTG; (**b**) activation energy by Kissinger method; and (**c**) TGA analysis.

**Table 4.** Comparative of soot catalytic combustion temperature with previous reports using carbon Vulcan as soot model.

| Sample | $T_m$ (°C) | Reference |
|---|---|---|
| $SrTiCuO_3$ | 596 | [9] |
| $Cu/SrTiO_3$ | 607 | [9] |
| $SrTiO_3$ | 650 | [9] |
| $SrKTiO_3$ | 582 | [22] |
| $SrKTiCuO_3$ | 600 | [22] |
| $LaFeO_3$ | 560 | [31] |
| $La_{0.7}Sr_{0.3}Co_{0.2}Fe_{0.8}O_{3-\delta}$ | 590 | [32] |
| Mn0 | 617 | This work |
| Mn1 | 591 | This work |

Figure 6 shows a representative image of the proposed mechanism. At low temperatures, adsorbed oxygen species seems to be the main contributing parameter, as previously reported [13]. Mn reductive species segregated as $Mn_3O_4$ in the Mn8 sample are able to adsorb and dissociate oxygen from the air to the soot–catalyst interface (blue arrow in Figure 6) which, together with the hydroxyl

species desorbed from the surface of the catalyst, drives the mass loss at low temperatures, as shown in Figure 5c. For Mn1 and Mn4, the existence of $Ti^{3+}$ and $Mn^{3+}$ are responsible for adsorbing oxygen from the air. By increasing the temperature, oxygen migrates from the bulk to the surface, enhanced by the redox pair $Mn^{3+}/Mn^{4+}$ and the existence of $Ti^{3+}/Ti^{4+}$ species (Red arrow in Figure 6). Mn1, with high $Mn^{3+}$ content and oxygen vacancies, can transport oxygen from the bulk to the surface and enhance the soot oxidation rate (Green arrow in Figure 6) [13,27]. Another possibility causing the behavior observed in Figure 5c is the better dispersion of Mn species on the surface of Mn1 and Mn4 catalysts against Mn8. By increasing the content of Mn in the Mn8 sample, agglomerates of $Mn_3O_4$ on the surface of the catalyst decrease the catalytic activity of these samples, as shown in Figure 5a and Table 3.

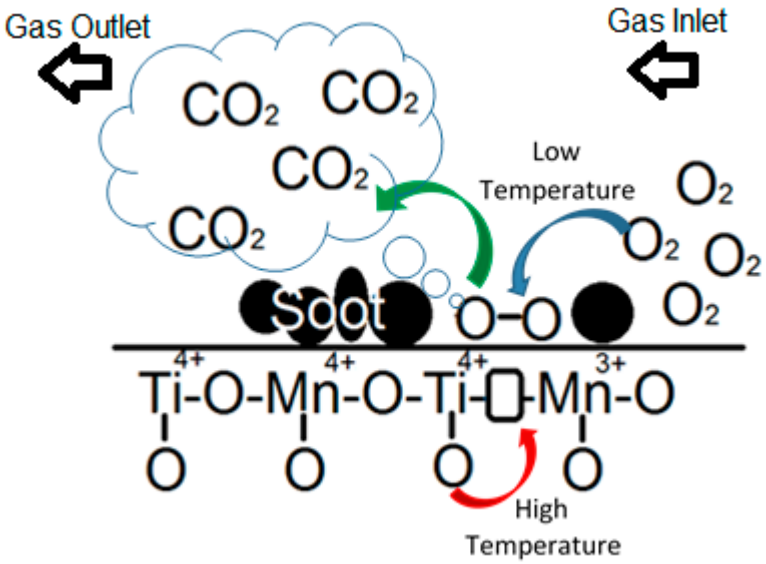


**Figure 6.** Scheme of soot catalytic oxidation over Mn doped $SrTiO_3$ catalyst.

## 3. Materials and Methods

### *3.1. Preparation of Catalyst*

Doped and undoped samples of $SrTiO_3$ were prepared by the hydrothermal method using titanium butoxide (>97%, Sigma Aldrich Co., St. Louis, MO, USA) and $Sr(NO_3)_2$ (>99%, Sigma Aldrich Co., St. Louis, MO, USA) as precursors. These reagents were mixed in stoichiometric ratios with 60 mL of 0.2 M NaOH to obtain a homogeneous solution. In the case of doped samples, the required amount of $Mn(NO_3)_2{\cdot}4H_2O$ (>97%, Sigma Aldrich Co., St. Louis, MO, USA) to prepare 1, 4, and 8 wt % of the doped metal was added. After mixing for 10 min., the final solution was placed into a Teflon vessel with 100 mL of volume and was hydrothermally treated at 180 °C for 24 h. After the thermal treatment, the solution was removed from the furnace and cooled to room temperature. The resulting precipitate was separated from the solution via decantation and washed gently with distilled water till a neutral pH was achieved. Finally, the powder was dried at 105 °C for 6 h and calcined at 600 °C for 5 h under ambient air with heating and cooling rates of 5 °C·$min^{-1}$.

### *3.2. Catalysts Characterization*

The phase composition of the perovskites was evaluated by X-ray diffraction (XRD) in a Siemens D-5000 diffractometer (Munich, Germany) with CuKα radiation (λ = 1.5418 Å) with a scanning and

step size of 0.5 s and 0.02°, respectively. The mean crystallite size ($d_s$) of the perovskites was calculated using the Scherrer equation (Equation (1)) [24]

$$d_s = \frac{k \times \lambda}{\beta \times \cos(\theta)} \quad (1)$$

where $d_s$ is the mean crystallite size, $k$ is the shape factor (0.9), λ is the X-ray wavelength (1.54 Å), $\beta$ is the broadening at half of the maximum intensity (FWHM), and $\theta$ is the Bragg angle. The lattice parameters were calculated from the peak (110) using the equation for cubic structure. The morphology, particle size and elemental composition were observed by scanning electron microscopy (SEM-EDS) 6490 LV JEOL Ltd. (Tokyo, Japan). $N_2$ adsorption-desorption isotherms were carried out at −196 °C, before the analysis, all samples were degassed at 300 °C for 1 h, the surface area was obtained by $N_2$ physisorption and calculated using the Brunauer–Emmett–Teller (BET) method using a Quantachrome Instruments Auto-sorb 3B equipment (Boynton Beach, FL, USA). X-ray photoelectron spectroscopy analysis (XPS) were performed on a K-Alpha$^{TM}$+ X-ray Spectrophotometer Thermo Scientific Inc. (Waltham, MA, USA) with a monochromatized Al Kα X-ray source (1486.7 eV) and passing energy of 40 eV. C 1s (binding energy 284.8 eV) of formed carbon was used as a reference. XPS spectra were deconvoluted using advantage software Avantage Thermo Scientific and Gaussian–Lorentzian and Shirley background. The content of Mn as doped metal was measured at wavelength of 294.93 nm by inductively coupled plasma–optical emission spectroscopy (ICP-OES) using Optima 4300 DV, Perkin Elmer Inc. (Waltham, MA, USA) equipped with AS-90 Autosampler (Waltham, MA, USA). For this measurement 1 g of each catalyst was dissolved in 10 mL of hot sulfuric acid and then diluted to 100 mL with distilled water.

### *3.3. Catalytic Test*

The catalytic assays for the soot oxidation reaction were carried out by mixing catalyst with carbon Vulcan (XC72R Cabot Corp., Boston, MA, USA), which was used as a soot model, in a 9:1 mass ratio. These reactants were previously mixed during 10 min. in an agate mortar using acetone as the organic solvent to ensure tight contact at the soot–catalyst inerface. Then, each mixture was placed in an alumina crucible for catalytic experiments. All experiments were carried out by DTA-DSC-TGA (STA 6000 Perkin Elmer Inc., Waltham, MA, USA) from room temperature to 850 °C at 5 °C/min with a flow rate of 50 mL/min of dry air. The temperature of maximal soot combustion, determined by DTG, in addition with the weight loss, determined by thermogravimetric analysis (TGA), were used to evaluate the catalytic performance. In addition, carbon mixed with inert material ($SiO_2$), with the same mass ratio (9:1), was also measured as a reference, un-catalyzed sample. Catalytic activity was determined by calculating the activation energy using the Kissinger equation [33], shown in Equation (2)

$$\frac{\ln \Phi}{T_p^2} = \frac{-E_a}{RT_p} + C \quad (2)$$

where Φ is the heating rate (5, 10, 20 or 40 K·min$^{-1}$); $T_p$ is the temperature in K at the maximum peak observed by DSC analysis; $R$ is the universal gas constant in J·mol$^{-1}$·K$^{-1}$; and $C$ corresponds to an experimental constant which is a function of the pre-exponential factor of the crystallization process $K_0$, the activation energy and the universal gas constant $R$.

## 4. Conclusions

A series of Mn-doped $SrTiO_3$ perovskites with varying ratios of Mn and distinct structures and dendritic morphologies were synthesized by the hydrothermal method. The incorporation of Mn into the structure was demonstrated for samples doped with Mn ≤ 4 wt % with $Mn^{4+}$ and $Mn^{3+}$ species in Ti sites. $Mn^{3+}$ in the structure promotes the oxygen surface adsorbed species. However, by increasing the amount of the metal dopant, the formation of manganese oxides segregated on the

surface, promoted the existence of $O_{lat}$. These segregated oxides lead to a decrease in the catalytic activity, which is attributed to the lower structural defects and reductive $Mn^{2+}$ species on the surface of this sample. The catalyst with the lowest $T_m$ and $E_a$ is the one doped by 1 wt % of Mn, which is attributed to the $Mn^{3+}/Mn^{4+}$ ratio characteristic of this sample, promoting the formation of oxygen surface adsorbed species caused by the presence of structural defects which also contribute to the mobility of the oxygen bulk to the surface as temperatures above the 500 °C.

**Acknowledgments:** The authors thank the Materials Construction Laboratory from FIC-UANL for their assistance in TGA-DSC measurements and MC. Daniel Gomez Ibarra and Adolfo Caballero from PGJ-NL for their support in the ICP analysis. In addition, S. Suárez-Vázquez thanks the projects PROMEP DSA/103.5/16/10510 and PAICYT IT510-10 for their partial financial support and UANL-"Impulso a la producción científica de jóvenes investigadores" for the partial financial support to publish this paper.

**Author Contributions:** S.I.S.-V. and A.C.-L. conceived and designed the experiments; C.M.-S. and S.I.S.-V. performed the experiments and analyzed the data; A.I.S.-V. performed and analyzed XRD experiments; C.E.M.-G. contributed reagents/materials/analysis tools; S.I.S.-V. wrote the manuscript.

**Conflicts of Interest:** The authors declare no conflict of interest.

## References

1. Fino, D.; Russo, N.; Saracco, G.; Specchia, V. The role of suprafacial oxygen in some perovskites for the catalytic combustion of soot. *J. Catal.* **2003**, *217*, 367–375. [CrossRef]
2. US-EPA. *Office of Transportation and Air Quality*; EPA-420-F-00-100; US-EPA: Washington, DC, USA, 2000.
3. Wang, Z.; Zhu, H.; Ai, L.; Liu, X.; Lv, M.; Wang, L.; Ma, Z.; Zhang, Z. Catalytic combustion of soot particulates over rare-earth substituted $Ln_2Sn_2O_7$ pyrochlores (Ln = La, Nd and Sm). *J. Colloid Interface Sci.* **2016**, *478*, 209–216. [CrossRef] [PubMed]
4. Hu, J.; Hu, Z.; Zhang, J.; Shuai, S. Effects of a catalyst on the nanostructure and reactivity of soot under an oxygen atmosphere. *Energy Fuel* **2016**, *30*, 2434–2442. [CrossRef]
5. Liu, S.; Wu, X.; Weng, D.; Li, M.; Ran, R. Roles of acid sites on Pt/H-ZSM5 catalyst in catalytic oxidation of diesel soot. *ACS Catal.* **2015**, *5*, 909–919. [CrossRef]
6. Liu, S.; Wu, X.; Weng, D.; Ran, R. $NO_x$-assisted soot oxidation on Pt-Mg/$Al_2O_3$ catalysts: Magnesium precursor, Pt particle size, and Pt-Mg interaction. *Ind. Eng. Chem. Res.* **2012**, *51*, 2271–2279.
7. Ura, B.; Trawzcynski, J.; Kotarba, A.; Bieniasz, W.; Illan-Gomez, M.J.; Bueno-Lopez, A.; Lopez-Suarez, F.E. Effect of potassium addition on catalytic activity of $SrTiO_3$ catalyst for diesel soot combustion. *Appl. Catal. B* **2011**, *101*, 169–175. [CrossRef]
8. Lopez-Suarez, F.E.; Bueno-Lopez, A.; Illan-Gomez, M.J.; Adamski, A.; Ura, B.; Trawczynski, J. Copper catalysts for soot oxidation: Alumina versus perovskite supports. *Environ. Sci. Technol.* **2008**, *42*, 7670–7675. [CrossRef] [PubMed]
9. Lopez-Suarez, F.E.; Parres-Esclapez, S.; Bueno-Lopez, A.; Illan-Gomez, M.J.; Ura, B.; Trawczynski, J. Role of Surface and lattice copper species in copper-containing (Mg/Sr)$TiO_3$ peroskite catalysts for soot combustion. *Appl. Catal. B* **2009**, *93*, 82–89. [CrossRef]
10. Feng, N.; Wu, Y.; Meng, J.; Chen, C.; Wang, L.; Wan, H.; Guan, G. Catalytic combustion of soot over Ce and Co substituted three-dimensionally ordered macroporous $La_{1-x}Ce_XFe_{1-y}Co_xO_3$ perovskite catalysts. *RSC Adv.* **2015**, *5*, 91609–91618. [CrossRef]
11. Feng, N.; Meng, J.; Wu, Y.; Chen, C.; Wang, L.; Gao, L.; Wan, H.; Guan, G. $KNO_3$ supported on three-dimensionally ordered macroporous $La_{0.8}Ce_{0.2}Mn_{1-x}Fe_XO_3$ for soot removal. *Catal. Sci. Technol.* **2016**, *6*, 2930–2941. [CrossRef]
12. Pecchi, G.; Dinamarca, R.; Campos, C.M.; Garcia, X.; Jimenez, R.; Fierro, J.L. Soot oxidation on silver-substituted $LaMn_{0.9}Co_{0.1}O_3$ perovskites. *Ind. Eng. Chem. Res.* **2014**, *53*, 10090–10096. [CrossRef]
13. Hernandez, W.Y.; Tsampas, M.N.; Zhao, C.; Boreave, A.; Bosselet, F.; Vernoux, P. La/Sr-based perovskites as soot oxidation catalysts for gasoline particulate filters. *Catal. Today* **2015**, *258*, 525–534. [CrossRef]
14. Dhakad, M.; Rayalu, S.S.; Kumar, R.; Doggali, P.; Bakardjieva, S.; Subrt, J.; Mitsubishi, T.; Haneda, H.; Labhsetwar, N. Low cost, ceria promoted perovskite type catalysts for diesel soot oxidation. *Catal. Lett.* **2008**, *121*, 137–143. [CrossRef]

15. Kim, C.; Qi, G.; Dahlberg, K.; Li, W. Strontium-doped perovskites rival platinum catalysts for treating $NO_x$ in simulated diesel exhaust. *Science* **2010**, *327*, 1624–1627. [CrossRef] [PubMed]
16. Shao, W.; Wang, Z.; Zhang, X.; Wang, L.; Ma, Z.; Li, Q.; Zhang, Z. Promotion effects of cesium on perovskite oxides for catalytic soot combustion. *Catal. Lett.* **2016**, *146*, 1397–1407. [CrossRef]
17. Sun, X.; Lin, J. Synergetic effects of thermal and photo-catalysis in purification of dye water over $SrTi_{1-x}Mn_xO_3$ solid solutions. *J. Phys. Chem. C* **2009**, *113*, 4970–4975. [CrossRef]
18. Wu, G.; Li, P.; Xu, D.; Luo, B.; Hong, Y.; Shi, W.; Liu, C. Hydrothermal synthesis and visible-light-driven photocatalytic degradation for tetracycline of Mn-doped $SrTiO_3$ nanocubes. *Appl. Surf. Sci.* **2015**, *333*, 39–47. [CrossRef]
19. Giroir-Fendler, A.; Gil, S.; Baylet, A. $(La_{0.8}A_{0.2})MnO_3$ (A = Sr,K) perovskite catalysts for NO and $C_{10}H_{22}$ oxidation and selective reduction of NO by $C_{10}H_{22}$. *Chin. J. Catal.* **2014**, *35*, 1299–1304. [CrossRef]
20. Peña, M.A.; Fierro, J.L.G. Chemical structures and performance of perovskites oxides. *Chem. Rev.* **2001**, *101*, 1981–2017. [CrossRef] [PubMed]
21. Zhang, L.; Nie, Y.; Hu, C.; Qu, J. Enhanced fenton degradation of Rhodamine B over nanoscaled Cu-doped $LaTiO_3$ perovskite. *J. Appl. Catal. B* **2012**, *125*, 418–424. [CrossRef]
22. Lopez-Suarez, F.E.; Bueno-Lopez, A.; Illan-Gomez, M.J.; Trawczynski, J. Potassium-copper perovskite catalysts for mild temperature diesel soot combustion. *Appl. Catal. A* **2014**, *485*, 214–221. [CrossRef]
23. Lencka, M.M.; Riman, R.E. Thermodynamic modeling of hydrothermal synthesis of ceramic powders. *Chem. Mater.* **1993**, *5*, 61–70. [CrossRef]
24. Suárez-Vázquez, S.I.; Gil, S.; García-Vargas, J.M.; Cruz-López, A.; Giroir-Fendler, A. Catalytic oxidation of toluene by $SrTi_{1-x}B_xO_3$ (B = Cu and Mn) with dendritic morphology synthesized by one pot hydrothermal route. *Appl. Catal. B* **2018**, *223*, 201–208. [CrossRef]
25. Kalyani, V.; Vasile, B.S.; Ianculescu, A.; Testino, A.; Carino, A.; Buscaglia, M.T.; Buscaglia, V.; Nanni, P. Hydrothermal synthesis of $SrTiO_3$: Role of interfaces. *Cryst. Growth Des.* **2015**, *15*, 5712–5725. [CrossRef]
26. Liu, Y.; Dai, H.; Du, Y.; Deng, J.; Zhang, L.; Zao, Z.; Au, C.T. Controlled preparation and high catalytic performance of three-dimensionally ordered macroporous $LaMnO_3$ with nanovoid skeletons for the combustion of toluene. *J. Catal.* **2012**, *287*, 149–160. [CrossRef]
27. Lin, X.; Li, S.; He, H.; Wu, Z.; Wu, J.; Chen, L.; Ye, D. Evolution of oxygen vacancies in $MnO_x$-$CeO_2$ mixed oxides for soot oxidation. *Appl. Catal. B* **2018**, *223*, 91–102. [CrossRef]
28. Giroir-Fendler, A.; Alves-Fortunato, M.; Richard, M.; Wang, C.; Díaz, J.A.; Gil, S.; Zhang, C.; Can, F.; Bion, N.; Guo, Y. Synthesis of oxide supported $LaMnO_3$ perovskites to enhance yields in toluene combustion. *Appl. Catal. B* **2016**, *180*, 29–37. [CrossRef]
29. Fang, S.; Wang, L.; Sun, Z.; Feng, N.; Shen, C.; Lin, P.; Wan, H.; Guan, G. Catalytic removal of diesel soot particulates over K and Mg substituted $La_{1-x}K_xCo_{1-y}Mg_yO_3$ perovskite oxides. *Catal. Commun.* **2014**, *49*, 15–19. [CrossRef]
30. Han, X.; Wang, Y.; Hao, H.; Guo, R.; Hu, Y.; Jiang, W. $Ce_{1-x}La_xO_y$ solid solution prepared from mixed rare earth chloride for soot oxidation. *J. Rare Earth* **2016**, *34*, 590–596. [CrossRef]
31. Xiao, P.; Zhong, L.; Zhu, J.; Hong, J.; Li, J.; Li, H.; Zhu, Y. CO and soot oxidation over macroporous perovskite $LaFeO_3$. *Catal. Today* **2015**, *258*, 660–667. [CrossRef]
32. Lee, C.; Jeon, Y.; Hata, S.; Park, J.; Akiyoshi, R.; Saito, H.; Teraoka, Y.; Shul, Y.; Einaga, H. Three-dimensional arrangements of perovskite-type oxide nano-fiber webs for effective soot oxidation. *Appl. Catal. B* **2016**, *191*, 157–164. [CrossRef]
33. Kissinger, H.E. Reaction kinetics in differential thermal analysis. *Anal. Chem.* **1957**, *29*, 1702–1706. [CrossRef]